

Proposal to Measure the Cross Section of NC Inclusive π^0 Interaction Channel

Ariana Hackenburg

Yale University

ariana.hackenburg@yale.edu

January 31, 2017



Contents

1	Introduction	6
2	Brief History of Neutrinos	6
2.1	Solar Neutrino Problem	6
2.2	LSND and MiniBooNE	8
2.3	Theory	9
2.4	Neutrino-Induced Charged Current π^0	9
3	Hardware	12
3.1	Booster Neutrino Beamline	12
3.1.1	Proton Acceleration	12
3.1.2	Beam Target and Horn	12
3.1.3	Neutrino Beam	13
3.2	The MicroBooNE Detector	14
3.2.1	Cryogenics	14
3.2.2	High Voltage	16
3.2.3	Wire Planes	16
3.2.4	PMTs	17
4	Software	18
4.1	Simulation	18
4.1.1	Genie and the Booster Neutrino Beam	18
4.1.2	Geant, NuWro, and the Interactions	18
4.1.3	Detector	18
4.1.4	Hardware + Software Triggers - (Neutrino Note)	18
4.2	Reconstruction	18
4.2.1	OpenCV Clustering	18

4.2.2	Cluster Matching	20
4.2.3	Shower Reconstruction	21
4.3	Energy Reconstruction	22
4.4	π^0 Reconstruction	24
4.5	Successfully Reconstructed Events	24
5	Event Selection	27
5.1	Hit Removal	27
5.2	$N\pi^0$ Filter	28
6	Cross Section Calculation	32
6.1	True Cross Section	32
6.2	Cross Section Calculation	34
A	Appendix	37

List of Figures

1	John Bahcall's Standard Solar Flux Model	7
2	Low energy excesses seen by the LSND (left) and MiniBooNE (right) experiments	8
3	a) Accelerator complex at Fermilab. Protons are accelerated to 8 GeV in the Booster before slamming into a Beryllium target; b) The target assembly used by MicroBooNE, with beam striking the slugs from the left.	13
4	The Booster complex as seen from above ground; MicroBooNE is situated at 470 m from the target, with MiniBooNE nearby.	14
5	3D model of the MicroBooNE's cryogenics system including pumps, filters, cooling system and monitors.	16
6	MicroBooNE was designed with these described contaminant limits in mind.	16

7	New π^0 ROI around ν_μ CC Selection II tagged pandora vertex.	18
8	Example from OpenCV online manual depicting polar transformation algorithm	19
9	a) The start point finding algorithm uses the ROI vertex to determine the which segment the start point lies in b) Depiction of flashlight merging algorithm. Flashlights (gray) are merged when they overlap. The trunk of the base flashlight is pinched at the start point to prevent over-merging near the vertex. A convex hull (red) is calculated over all final flashlights to form the new cluster boundaries.	21
10	3D reconstructed showers are projected back into 2D as a visual sanity check that shower reconstruction is successful.	22
11	True CC π^0 's selected and successfully reconstructed through the full chain in MCC7 BNB + cosmics sample.	25
13	MicroBooNE the model and MicroBooNE the real man. (Right) Taken when the TPC was slid into the cryostat December 2013.	25
12	Calculated mass peak for the 585 selected CC π^0 events.	26
14	Charged Current event with nucleons interacting via Meson Exchange Current (MEC)	26
15	Vertex is depicted in cyan in both views. a) Before hit removal (left) and b) After hit removal (right) only shower-like hits originating from vertex remain.	28
17	π^0 ratio plots constructed by taking the ratio of shower-like charge to total charge in radius = 60cm a) Absolute scale with corresponding efficiency, purity and product; b) Same plot area normalized to give a sense of the distribution shapes.	29
16	Ratio plots constructed by taking the ratio of shower-like charge to total charge at various radii.	30

18	π^0 ratio plots constructed by taking the ratio of shower-like charge to total charge minus charge associated with the muon in radius = 60cm a) Absolute scale with corresponding efficiency, purity and product; b) Same plot area normalized to give sense distribution shapes.	31
19	ν_μ Flux from Booster Neutrino Beam (BNB) at 470m	33
20	Genie calculated CC π^0 cross section. The cross sections are calculated at various energies for both Carbon and Argon, and for signal definitions that include mesons in the final state and those that don't. The MiniBooNE measured cross section is displayed along with the MicroBooNE MC calculated cross section.	34

1 Introduction

2 Brief History of Neutrinos

Definitive proof for neutrino oscillation has been delivered over and again in the last 15 years. Alongside this proof however, have come several notoriously anomalous results. In this section, we explore some of these anomalous results and their impact on the present state of neutrino physics.

2.1 Solar Neutrino Problem

Any sort of historical review of neutrino physics at some point comes to Ray Davis, and so we might as well start our story here. In the late 1960s, Ray Davis of Brookhaven National Lab (BNL) ventured 4850ft underground in the Homestake mine with a plan to measure various contributions to solar neutrino flux [1]. Working closely with John Bahcall's theory team at CalTech, Davis' group built a tetrachloroethylene detector sensitive down to 0.814 MeV and primarily to B^8 solar neutrinos[1] a mile underground in Homestake Mine. In 1968, the group released results which revealed that a fraction of the predicted solar neutrinos were missing. This result became known as "the solar neutrino problem".

The Homestake experiment ran for 20 years, with results through the duration pointing to the same conclusion: 2/3 of the neutrinos predicted by Bahcall's Standard Solar Model (Figure 1) were not accounted for in the data[1]. Throughout the 80's and 90's, a series of experimental results from various collaborations confirmed the mysterious lack of solar neutrinos [2] [3] [9]. Kamiokande II¹, a 3 kton water Cherenkov detector built in Japan in the 80s, was only sensitive to B^8 neutrinos above 6 MeV[3] because of the surrounding radioactivity. Despite its inability to probe the keV energies of the Homestake experiment,

¹The original Kamiokande focused primarily on proton decay. After initial data taking, adjustments were made to the original detector in order to make it sensitive enough to study electron recoils from elastic neutrino scatters in water. One example addition was a surrounding layer of water which was intended to decrease background radiation. This "new" experiment was called Kamiokande II

Kamiokande II was a highly appealing detector due to its real time depiction of events and its ability to reconstruct both the energies and directions of those events[3]. Due to the unique ability of this detector, Kamiokande II was able to for the first time conclude that neutrinos were coming from the sun. In addition to this remarkable discovery, Kamiokande II also observed an apparent lack of solar neutrinos.

A quick recap at this point would indicate something a bit unsettling about our story thus far. The Davis experiment began digging into Bahcall's models in the 60s; yet here we were in the 90s with still no verified explanation of what was causing the observed neutrino deficit. Were neutrinos oscillating? Was something wrong with the sun[8]?

Quick to follow suit was the Sudbury Neutrino Observatory (SNO) in 2002. SNO was a 1 ktonne spherical deuterium Cherenkov detector located 6800ft under ground in the Creighton Mine in Sudbury[9]. The greatest barrier experiments before SNO had faced in detecting ν_μ or ν_τ interactions was that the μ and τ are heavier (105 MeV and 1777 MeV respectively) than the energy of the solar neutrino spectrum, which only extends to about 30MeV. Deuterium, which replaces the hydrogen in water with a proton and a neutron, has a dissociation energy of 2 MeV. This fact uniquely equipped SNO to measure the flux of all three neutrino flavors[9]—this total flux matched shockingly well with Bahcall's predictions in his SSM. SNO had conclusively solved the solar neutrino problem.

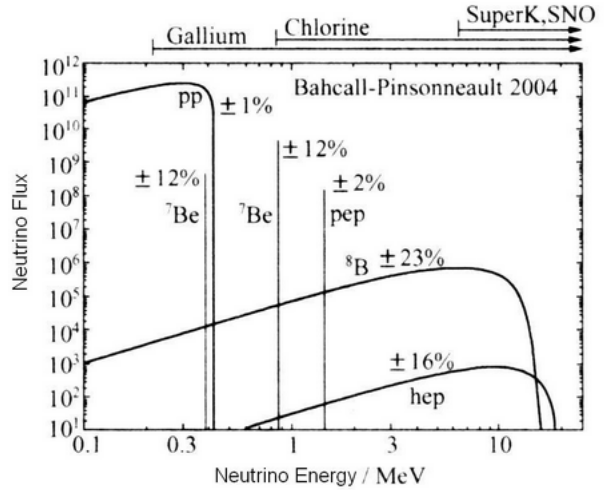


Figure 1: John Bahcall's Standard Solar Flux Model

2.2 LSND and MiniBooNE

In the last 20 years, a variety of other experimental results have indicated that the 3-neutrino oscillation model (and thus, the Standard Model), may not be complete. Liquid Scintillator Neutrino Detector (LSND), a scintillation detector in a stopped pion beam from the 90's, expected the majority of its events to come from ν_μ and $\bar{\nu}_\mu$, with a small fraction of $\bar{\nu}_e$ interactions—in their results, they observed an excess of low energy electron anti-neutrino events for $\frac{L}{E} \sim 1 \frac{m}{MeV}$ (Figure 2), explained at the time with a simple 2-neutrino oscillation model [13]. These unexpected results led to the construction of the Mini Booster Neutrino Experiment (MiniBooNE), a Cherenkov detector in Booster Neutrino Beam (BNB) at Fermilab. After 10 years of running, MiniBooNE's data revealed an excess of low energy events in both neutrino and anti-neutrino modes at energies below and incorporating LSND's data (Figure 2)². These results did a couple important things: first, MiniBooNE's data refuted the previous 2-neutrino oscillation explanation [12], and second, it called into question the nature of the observed low-energy excess. This is the question MicroBooNE resolves to answer, and where my story begins.

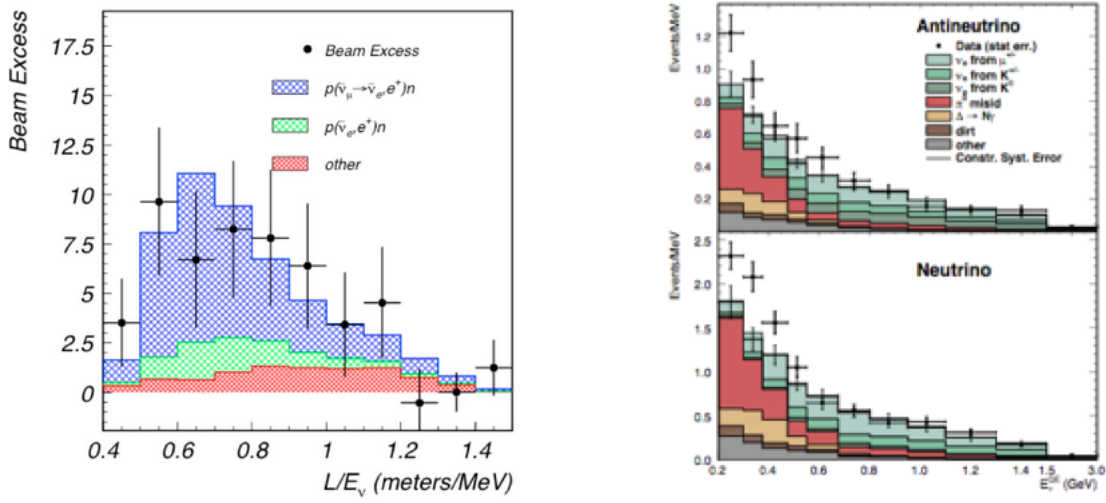


Figure 2: Low energy excesses seen by the LSND (left) and MiniBooNE (right) experiments

²MiniBooNE also observed different amounts of excess in neutrino and anti-neutrino mode, leading to additional questions about nuclear interactions, cross sections and the relationship between the neutrino and antineutrino[12]

2.3 Theory

Each neutrino flavor (ν_e, ν_μ, ν_τ) can be written as a linear combination of 3 mass eigenstates with the use of a unitary rotation matrix. It is most convenient to begin by looking at a simplified 2 neutrino oscillation model:

$$|\nu_x\rangle = \sum_{j=1,2} U_{ij} |\nu_j\rangle \quad (1)$$

Using the time-dependent Hamiltonian of the system, we can derive a probability of oscillation from flavor α to flavor β (see Appendix A for more detail about this derivation). After propagating these states in time and doing some rearranging, we arrive at

$$P(\nu_\alpha \rightarrow \nu_\beta) = \sin^2(2\theta) \sin(1.27\Delta m^2 \frac{L}{E}) \quad (2)$$

where θ is the mixing angle of the oscillation, Δm^2 is the frequency of neutrino oscillation, L is the length the neutrino traveled and E is the energy of the neutrino at its source. It is clear then that $\frac{L}{E}$ is the experimentally controllable parameter—an experiment's choice of $\frac{L}{E}$ depends on the ranges Δm^2 and $\sin^2(2\theta)$ it wishes to probe.

It is useful to look at an example of how the free parameter affects sensitivity. An experiment is most sensitive to Δm^2 for $\Delta m^2 \approx E/L$. In addition, the neutrino beam diverges $\propto \frac{1}{L^2}$. So an experiment with a short baseline (small L) has the benefit of seeing lots of events (ie, has high sensitivity to $\sin^2(2\theta)$), and is sensitive only to large values of Δm^2 [11].

2.4 Neutrino-Induced Charged Current π^0

A number of previous measurements on the charged current (CC) π^0 cross section exist, and it is worth first understanding where the field is and how we can contribute to it.

In the 80's a number of CC π^0 cross section measurements were made by a variety of

different experiments. Argonne National Laboratory used a 12-ft bubble chamber full of hydrogen and deuterium to investigate single-pion production by the weak charged current [20] [21]. ANL examined a restricted energy range of $E_\nu \geq 1.5\text{GeV}$ in order to restrict multi- π backgrounds entering their final sample of 273 events. They measured the cross section as a function of energy. BNL performed similar studies in a 7ft deuterium bubble chamber in a broad band beam with average energy 1.6GeV. Their signal sample was bigger at 853 events, and spanned an energy range up to 3 GeV. A few other experiments made measurements at higher energies, above the range of MicroBooNE [23] [25].

More recently, several experiments at Fermilab have made this cross section measurement. In 2011, the MiniBooNE experiment, a Cherenkov detector filled with mineral oil that sits in the Booster Neutrino Beam (BNB), made cross section and differential cross section measurements of the charged current neutral π^0 interaction channel. They required their signal events to have an observed single μ^- , single π^0 , any number of additional nucleons, and no additional mesons or leptons. With 5810 signal events in their sample, they measured a flux-integrated cross section of $(9.2 \pm 0.3\text{stat.} \pm 1.5\text{syst.}) \times 10^{-39} \frac{\text{cm}^2}{\text{CH}_2}$ [26] [27].

From 2007-2008, SciBar Booster Neutrino Experiment at Fermilab (SciBooNE) took data in the Booster Neutrino Beam. In 2014, a SciBooNE thesis measurement showed a measured CC π^0 cross section of $(5.6 \pm 1.9_{fit} \pm 0.7_{fit} \pm 0.5_{int} - 0.7_{det}) \times 10^{-40} \frac{\text{cm}^2}{\text{nucleon}}$ with 141 signal data events. The signal definition employed was different than that used by MiniBooNE in that it allowed N additional mesons in its final state. Nevertheless, when the MiniBooNE result is scaled per nucleon, the results agree with one another [28].

Most recently in 2015, the Minerva experiment measured $\bar{\nu}_\mu$ charged current π^0 differential cross sections against a number of variables on polystyrene [29] [30]. Minerva lies in the Neutrinos at the Main Injector (NuMI) beamline at Fermilab, and probes an energy range of 2-10 GeV. While MicroBooNE lies in the BNB and will probe a lower energy range, we note that the measurement signal here is the same as MiniBooNE with the requirement of a μ^+ rather than a μ^- in the final state.

A final measurement of note is that of inclusive CC π^0 production cross section by K2K in 2011 [31]; this measurement is presented as a ratio measurement to CCQE.

MicroBooNE, like MiniBooNE and SciBooNE, lives in the BNB at Fermilab. In the remaining parts of this note, we will run our analysis with the high statistics MiniBooNE results in mind for direct comparison. This will be the first CC π^0 measurement on Argon.

3 Hardware

3.1 Booster Neutrino Beamline

The Booster Neutrino Beamline (BNB) is situated at Fermi National Laboratory in Batavia Illinois. The BNB delivers a neutrino beam to the MicroBooNE detector 470 m from the target through a series of acceleration, focusing, collimating. The various stages of the beam are described here.

3.1.1 Proton Acceleration

Neutrino beam creation begins with H^- ion production and acceleration to 750 keV in a Cockcroft-Walton DC accelerator [15]. The beam of H- ions are subsequently boosted to 400 MeV in a linear acceleration and stripped of their electrons before they enter the Booster [19]. The Booster operates at a cycle frequency of 15 Hz, while each RF cavity operates at 84x this rate. As the protons move through the various RF cavities, they are bunched into 81 buckets (3 of what would otherwise be 84 buckets are removed in order to preserve beam uniformity), where all buckets are separated by 19 ns, and all buckets are 2 ns in width. One collection of these 81 buckets is called a beam spill, lasts around $1.6 \mu s$ and typically consists of $1 - 5e12$ Protons On Target (POT). Spills are directed into the Booster Neutrino Beamline by a switch magnet, and steered to the target by a series of dipole and focusing-defocusing (FODO) quadrupole magnets. The configuration of this assembly is shown in Figure 3a.

3.1.2 Beam Target and Horn

At this point, the bunched protons are impinged on a Beryllium Target. The target consists of 7 Be slugs, 10 cm long, 1 cm in diameter, and is embedded at the front end of the Booster Horn (Figure 3b). The slugs are suspended in an outer Be tube by three Be fins placed equi-distanced around the tube. Air is circulated around the slugs and then passed across a heat exchanger before being recycled, to maintain the slugs at a constant

temperature. This temperature is monitored at all times, and the proton beam is shut off if any abnormality in temperature or radioactivity is detected. The location of the beam is calibrated with a multi-wire chambers to ensure that it is interacting with the target itself and not surrounding material. The beam's intensity and position are monitored consistently.

The result of proton collision with the Be is a spray of other particles which then pass into the magnetic focusing horn. The horn is made from aluminum alloy and consists of an inner conductor along which current runs in, and an outer conductor along which it returns. This configuration of current flow induces a toroidal magnetic field between the conductors, which enables the removal of charged particles: positive in Neutrino Mode, negative in Anti-Neutrino Mode. During this process, the horn heats up and needs to be cooled. Ports in the outer conductor allow nozzles to spray water onto the inner conductor, which then drains out the bottom of the horn.

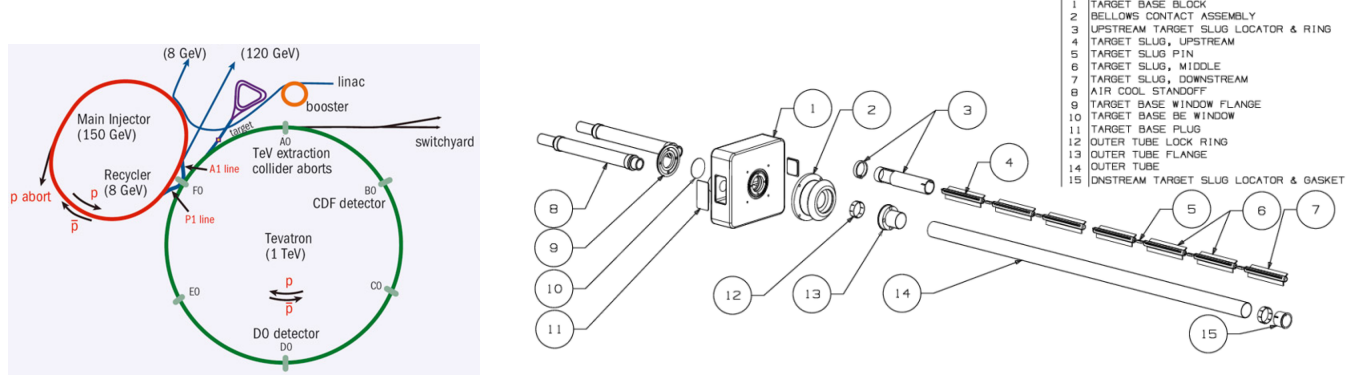


Figure 3: a) Accelerator complex at Fermilab. Protons are accelerated to 8 GeV in the Booster before slamming into a Beryllium target; b) The target assembly used by MicroBooNE, with beam striking the slugs from the left.

3.1.3 Neutrino Beam

The singularly charged beam now heads downstream to the collimator. This 214 cm of concrete sits 214 cm from the front of the target and acts as a dump for particles from secondary interactions which will not contribute to the neutrino flux of interest.

The remaining particles then enter the decay pipe. This 2 m wide pipe is made of corrugated steel, filled with air and packed into dolomite. In the 45 m length of the decay

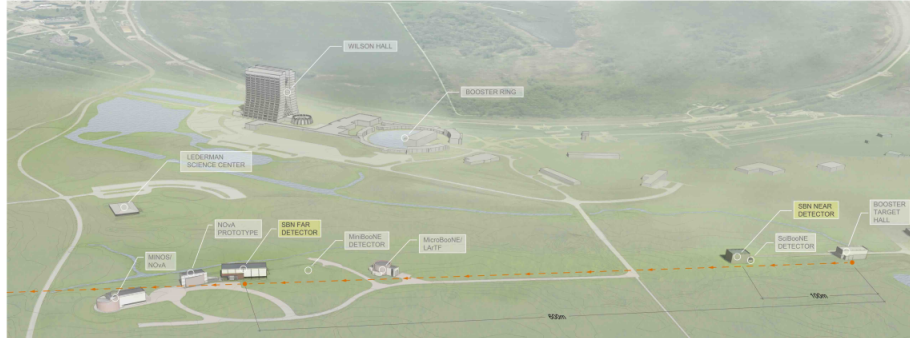


Figure 1. Aerial diagram showing location of MicroBooNE along the BNB (orange dashed line) at Fermilab.

Figure 4: The Booster complex as seen from above ground; MicroBooNE is situated at 470 m from the target, with MiniBooNE nearby.

pipe, π^+ from the initial proton-Be interaction will decay into μ^+ and ν_μ . A concrete and steel beam stop at the end of the decay pipe captures μ^+ 's, allowing only neutrinos to pass on. At this point, the neutrinos travel 470 m through the ground until they reach the MicroBooNE detector (Figure 4).

3.2 The MicroBooNE Detector

The Micro Booster Neutrino Experiment (MicroBooNE) is a Liquid Argon Time Projection chamber. Its various subsystems are described in detail below.

3.2.1 Cryogenics

MicroBooNE's cryostat is a type 304 stainless steel tube with inner diameter of 3.81 m, length of 12.2 m, and capacity of 170 tonnes. The stability of the detector medium has a large systematic impact on the data taken by MicroBooNE. For example, the drift velocity of electrons is dependent on both the temperature and pressure of the Liquid Argon (LAr), as well as its laminar and turbulent flow. Because the drift time and drift X coordinates only maintain a clear correlation when the drift velocity is well understood, it is crucial to set conditions under which this is the case. The expected drift velocity of electrons is 1600 $\frac{m}{s}$ at 500 $\frac{V}{cm}$ in LAr. In order to achieve a 0.1% consistency in drift velocity, the temperature

gradient must be controlled to within 0.1 K, and flow rate of LAr controlled to $1 \frac{m}{s}$. A layer of insulating foam around the cryostat prevents Liquid Argon from boiling off due to large temperature differences in surrounding materials. Additionally, 12 Resistive Thermal Devices (RTD) are used to consistently monitor the temperature of the detector at various locations. [32]

MicroBooNE also requires the LAr in the detector to be very pure to mitigate other systematic effects. These requirements include a 100 ppt O_2 contamination level, to ensure the proper detection of events that must traverse the full 2.5 m drift length, and a 2 ppm N_2 contamination level to minimize quenching of scintillation light from interactions. Additionally, the vessel is designed to minimize both outgassing by the detector walls and leakage through weld ports; contamination from these sources is cleaned and recycled using a purification system. The MicroBooNE purification system consists of 2 condensers (1 used primarily for backup), 2 pumps and 2 filters, and proceeds as follows: In the beginning, gaseous Argon leaves the detector and enters one of the condensers. Each condenser, designed to control the heat load on the detector, contains a liquid nitrogen coil over which the gaseous Argon passes before it's pumped through the filter in liquid form. Each condenser is designed to handle a load of 9.5 kW; this compares with the 6 kW heat load during a normal day of running the pumps and all electronics. The LAr is then pumped through 1 of 2 parallel filter skids, where each filter skid contains 2 filters. The first filter is a 4A molecular sieve tasked mainly with removing water from the Argon. The second filter removes O_2 and any remaining water; since this filter effectively removes water, it is placed after the first filter to avoid saturating the second filter with water contaminant and allowing the remaining O_2 to recirculate. Finally, the Argon is passed through a stainless steel particulate filter of grate width 10 microns to prevent any materials from the piping entering the detector.

The purity is monitored using double-gridded ion chambers ***REFERENCE. The monitors are effectively small TPCs: Q_C charge is generated at the cathode, the charge drifts in an applied electric field, and Q_A charge is detected at the anode. The ratio of these charges

is known as the electron lifetime given by the formula below:

$$\frac{Q_A}{Q_C} = e^{-\frac{t}{\tau}} \quad (3)$$

A purity monitor with a 50 cm drift lives directly downstream of the filters described above to test their effectiveness. 2 other monitors live in the detector itself, one at the cathode and one at the anode. These 2 monitors sit at different depths, to measure depth effect on lifetime. The MicroBooNE lifetime is consistently very high (how high???). The cryostat is maintained at the purity levels described in Figure 6.

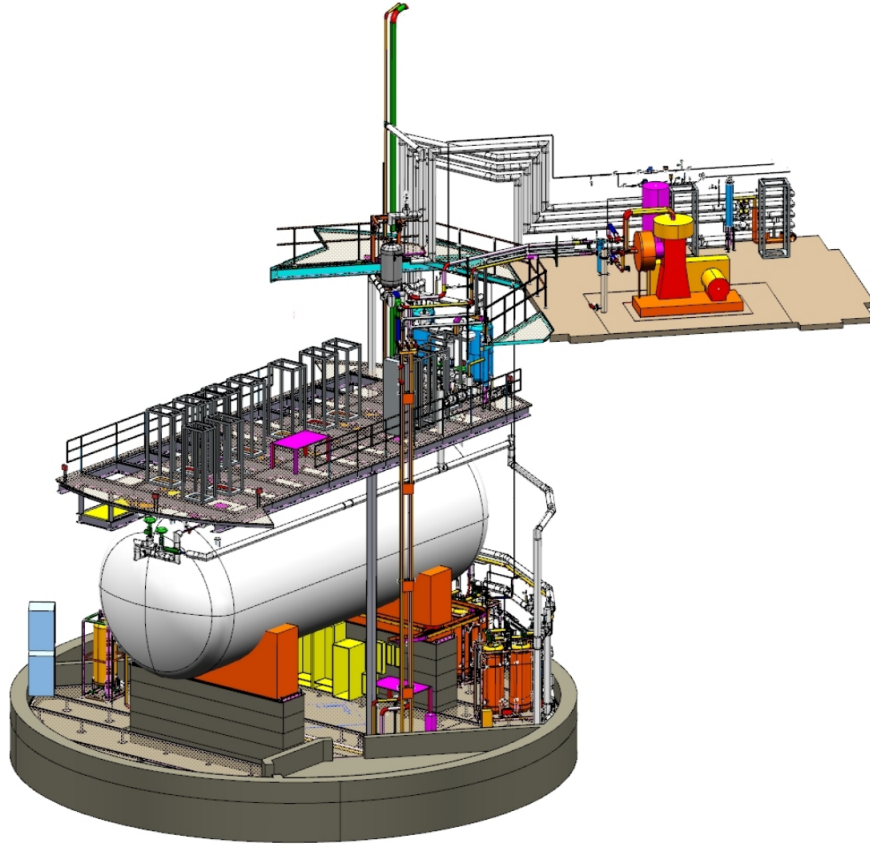


Figure 5: 3D model of the MicroBooNE’s cryogenics system including pumps, filters, cooling system and monitors.

Nitrogen Cooling:

Table 3. Primary design requirements for MicroBooNE cryogenic and purification systems.

Parameter	Value	Motivation
Argon purity	<100 ppt O ₂ equivalent	MIP identification at longest drift
Argon purity	<2 ppm N ₂	Scintillation light output
LAr temperature gradient	<0.1 K throughout volume	Drift-velocity uniformity
LAr recirculation rate	1 volume change/2.5 days	Maintain purity
Cryostat heat load	<15 W/m ²	Minimize convection and bubbles
Cryogenic cooling capacity	10 kW	Capacity for expected heat load
Cryostat max. operating pressure	2.1 bar	Determines relief sizing

Figure 6: MicroBooNE was designed with these described contaminant limits in mind.

3.2.2 High Voltage

3.2.3 Wire Planes

Ionization charge from interactions in MicroBooNE drifts in the applied electric field to t3 wire readout planes. The passing charge leaves induced pulses on the first 2 "induction" planes, and collects onto the final "collection" plane. The 2 induction planes are at 60 and -60 degrees to the vertical and contain 2400 150 μm gold-plated copper wires. The collection plane contains 3456 wires all perfectly vertical. Once charge is collected, signals from the wires are amplified and sent on to be stored analyzed.

3.2.4 PMTs

MicroBooNE relies on the fine grained calorimetric abilities of a LArTPC to do its reconstruction and particle ID. However, MicroBooNE is a surface detector and is subject to large number of cosmic backgrounds.

4 Software

4.1 Simulation

4.1.1 Genie and the Booster Neutrino Beam

4.1.2 Geant, NuWro, and the Interactions

4.1.3 Detector

4.1.4 Hardware + Software Triggers - (Neutrino Note)

4.2 Reconstruction

4.2.1 OpenCV Clustering

OpenCV is an open source computer vision library with functions to aid in pattern recognition and image processing. More on the framework and OpenCV tools developed previously are discussed in a previous technote [?]. Here we describe new algorithms developed to improve the selected sample size obtained from Neutrino 2016 efforts[?].

A number of links in the OpenCV clustering chain have been updated since Neutrino 2016. First, we no longer use Pandora shower reconstruction to find neutrino events containing π^0 . The vertex candidate associated with Selection II is used to build a simple ROI with constant 100cm bounds in every direction (Figure 7).

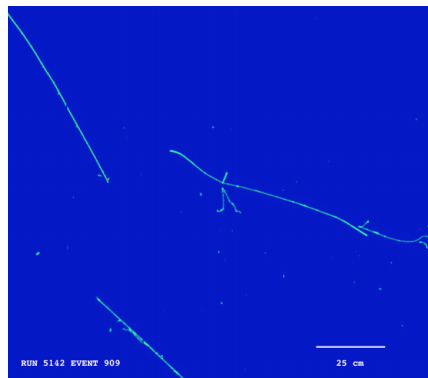


Figure 7: New π^0 ROI around ν_μ CC Selection II tagged pandora vertex.

Once the ROI has been built and track-like hits removed, clustering begins with a polar clustering algorithm (Figure 8) on the remaining hits. This algorithm operates by transforming image information into polar coordinates (with the origin set at the reconstructed vertex location), performing the same image manipulation described in [?], and transforming back. This strategy has the advantage over our previous simple image manipulations in that it enforces an image blur in the direction of showering. This prevents lateral over-merging in a number of events. From here we filter OpenCV defined clusters which pierce or lie outside of the previously defined ROI as they are likely not of interest to our reconstruction.

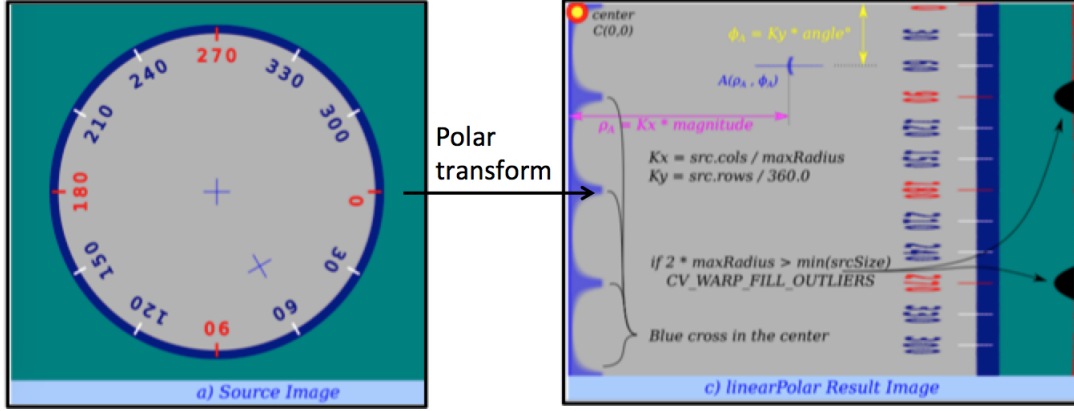


Figure 8: Example from OpenCV online manual depicting polar transformation algorithm

On this reduced set of clusters, we can now run parameter finding algorithms to assign each remaining cluster a start point and direction. Start point calculation is performed in the following way: each OpenCV calculated contour has an associated minimum bounding box that surrounds it (Figure 9a). The start point finding module segments this bounding box into 2 segments long ways. The algorithm then locates the hit of the cluster that is closest to the ROI vertex. The segment this hit belongs to is then chosen. Finally, within this chosen segment, we search for the hit furthest from the center of the minimum bounding box. In the adjacent segment, the hit furthest from the center is assigned to be the end point. We assign the cluster's direction to be the direction of the cluster's bounding box.

Now that our clusters have start points and directions we can attempt to combine charge which was not clustered together during polar clustering. We perform the merging on a

reduced image, removing all clusters with less than 10 hits. This removal prevents very small clusters from being merged with larger clusters and skewing our matching results later on. The algorithm we use to do the merging builds flashlight shapes around each cluster and combines hits when the flashlights overlap (Figure 9). The start point of the cluster closest to the ROI vertex is used as the start point for the new cluster, while the end point is reassigned to the new cluster hit furthest from the start point.

Finally, we apply 4 simple filters to reduce the number of bad/uninteresting clusters passing on to matching. First, we remove clusters with fewer than 10 hits. Next, we remove any clusters which are not aligned well with the vertex; this removes lingering cosmic rays and some misclustered hits. Occasionally when events are complicated (e.g. crossing muon, lot's of information, dead wires, etc.) the flashlight merging algorithm will over-merge. To prevent extreme overmerges from continuing on to the next stage, we filter clusters whose outer contour contains the vertex. The final filter is intended to prevent matching in planes with many dead wires. In order to avoid utilizing clusters reconstructed on a plane over a range which contains significant gaps due to “dead” or otherwise poorly-functioning wires, we assign a score to each plane’s ROI. Dead wires closer to the vertex have a stronger weight than those wires near the ROI boundaries. This score varies event-by-event and describes the percentage of the ROI which is covered by dead or bad wires. This algorithm enforces that Y plane clusters will always pass on to matching; the clusters in the remaining U or V plane with the highest plane score are passed on to matching.

4.2.2 Cluster Matching

Before we can reconstruct showers and start looking for π^0 ’s, we first need to match cluster pairs across planes. We do this by noting that time is a shared coordinate across planes and assigning scores to cluster pairs based on their agreement in time. We quantify this score using a measure denoted as the **Integral over Union**, or **IoU** for short. This

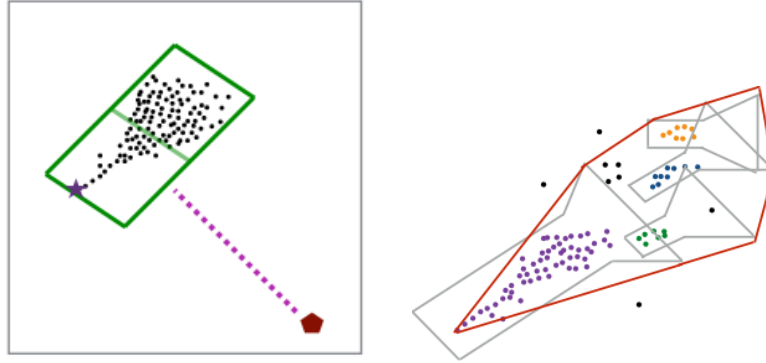


Figure 9: a) The start point finding algorithm uses the ROI vertex to determine which segment the start point lies in b) Depiction of flashlight merging algorithm. Flashlights (gray) are merged when they overlap. The trunk of the base flashlight is pinched at the start point to prevent over-merging near the vertex. A convex hull (red) is calculated over all final flashlights to form the new cluster boundaries.

quantity is defined as:

$$\text{IoU} = \frac{\Delta t_1 \cap \Delta t_2}{\Delta t_1 \cup \Delta t_2} \quad (4)$$

With Δt denoting the time-range associated to the hits in a given cluster. Clusters which do not overlap are assigned a score of -1, while those that do are assigned a score between 0 and 1, with 1 being perfect overlap. At the end of the consideration of all match permutations, the highest scores are used to create matched pairs until no clusters or viable match pairs remain. We require that there be at minimum a 25% agreement in time in order for a match to be made. We also require that one of the matched clusters come from the collection plane, as the collection plane is currently the plane used for calorimetry.

4.2.3 Shower Reconstruction

Shower reconstruction uses 2D information created during the previous matching stage to create one 3D object.

3D Direction We rely here on the reconstructed 3D interaction vertex to reconstruct the 2D projections. The 2D direction is computed as the charge-weighted average vector sum of

the 2D distance from the vertex to each hit in the cluster.

$$\hat{p}_{2D} = \sum_{i=0}^N \frac{r_i - r_{\text{vtx}}}{q_i} \quad (5)$$

With N denoting the number of hits in the cluster, r_i the position of the hit, q_i its charge, and r_{vtx} the position of the projected vertex. Given two 2D weighted directions, the 3D direction is calculated using geometric relations between the planes and clusters.

3D Start Point Reconstruction We calculate the 3D start point by finding the 3D overlap position of the OpenCV reconstructed 2D start points of the matched pair of clusters. The time tick coordinates from each cluster are averaged to calculate a 3D shared time coordinate. The (Y,Z) coordinates are identified by the intersection between the wires associated with 2D start points. Wires must intersect inside the TPC for a shower to be reconstructed.

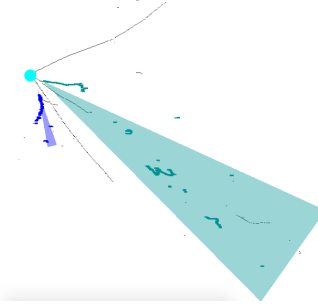


Figure 10: 3D reconstructed showers are projected back into 2D as a visual sanity check that shower reconstruction is successful.

4.3 Energy Reconstruction

The energy of each EM shower is reconstructed using a calorimetric energy measurement. This procedure is as follows: the integrated ADC charge measured for all the hits associated to an EM shower are converted, using a single, fixed constant value, to MeV accounting for the signal processing, electronics, and detector effects which transform deposited energy in the detector to digitized signals in our readout. For this work, only hits from the collection plane are used to reconstruct a shower's energy. The conversion from raw charge to MeV is

calculated as follows:

- **Electronics Gain:** A conversion from ADCs to number of electrons collected on a wire of $198 e^- / \text{ADC}$ is applied. This value is obtained by accounting for the specifications of the MicroBooNE electronics. See “Noise Characterization and Filtering in the MicroBooNE TPC” [?] for more details.
- **Lifetime Correction:** No lifetime correction is applied for data, given the exceptional Ar purity and high measured electron lifetime [?]. For MC, where an 8 ms lifetime is simulated, we correct the charge associated to each hit with an exponential correction given by $e^{t^{\text{ms}}/8^{\text{ms}}}$ where t is the drift-time associated to a hit (which we know thanks to the fact that we are reconstructing beam-induced π^0 s, generated at the trigger-time).
- **Argon Ionization:** The work function required to ionize an argon atom by a traversing charged particle is 23.6 eV, which we account for.
- **Ion Recombination:** The ionized charge which reaches the TPC wire-planes is a function of the deposited energy and the ion-recombination which quenches a fraction of the original ionization produced. Ion-recombination depends on the local density of positive and negative ions produced (and thus on the dE/dx of the particle), and on the strength of the local electric field. Electrons and photons have a smaller variation in dE/dx over the energy range of interest for MicroBooNE than for muons, pions, and protons. In addition, measuring the local dE/dx associated to an individual hit is challenging for EM showers, which consist of many branches of ionization propagating in different 3D directions. For these reasons, we apply a single, constant recombination correction of 0.38 obtained by assuming a fixed dE/dx of 2.3 MeV/cm and utilizing the Modified Box recombination model, as parametrized by the ArgoNeuT collaboration [?], applied at MicroBooNE’s electric field of 273 V/cm.

This gives us an energy calibration constant of:

$$198 \frac{e^-}{\text{ADC}} \times 23.6 \times 10^{-6} \frac{\text{MeV}}{e^-} \times \frac{1}{1 - 0.38} = 7.54 \times 10^{-2} \frac{\text{MeV}}{\text{ADC}} \quad (6)$$

4.4 π^0 Reconstruction

At this point we have some number of events that have made it through Selection II filter, hit removal, N- π^0 filter, OpenCV clustering and shower reconstruction. Now we can start checking events for π^0 's by examining properties of the reconstructed showers. Currently a 2-shower pair needs to satisfy several criteria in order to be considered a π^0 candidate. First, the impact parameter of the 2 showers must be $\leq 4\text{cm}$. Additionally, the 3D opening angle must be > 20 degrees; π^0 pairs with angles smaller than this tend to be cross-merged or overlapping. Finally, we require that the radiation length of the showers be $\leq 62\text{cm}$ with respect to the reconstructed vertex. If a pair of showers passes these criteria, they are considered to be a π^0 candidate. We do not currently handle the case where more than one viable candidate pair per event is found; these cases are simply neglected for now. We also do not include an energy or mass peak cut at this time; we hope to include these cuts in the future once we've understood our calibration scale better.

4.5 Successfully Reconstructed Events

The result of our reconstruction + selection chain is 585 CC π^0 candidate events. The breakdown of these events is described in the next section. Figure 11 shows a few examples of candidates in our sample. As a sanity check, we calculate the mass value of each pair in Figure 12.

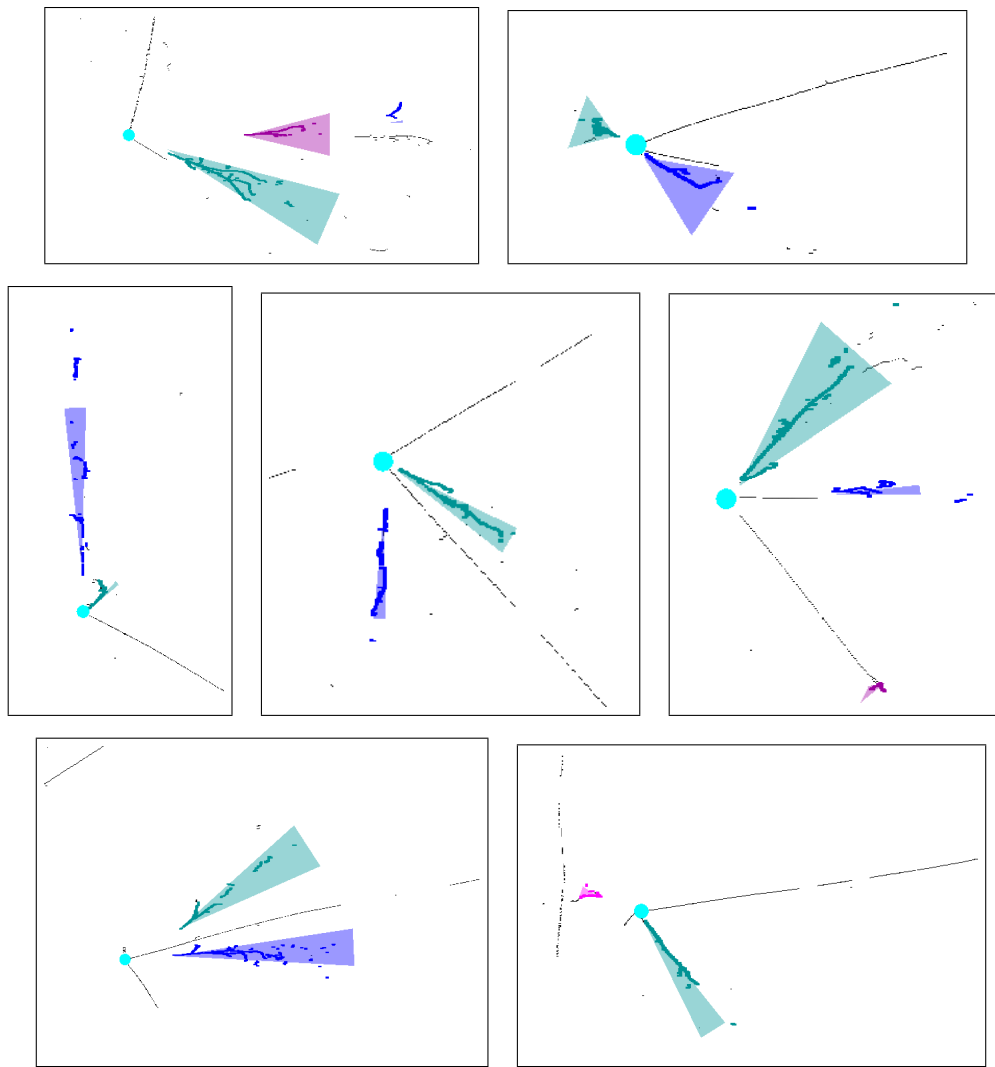


Figure 11: True CC π^0 's selected and successfully reconstructed through the full chain in MCC7 BNB + cosmics sample.

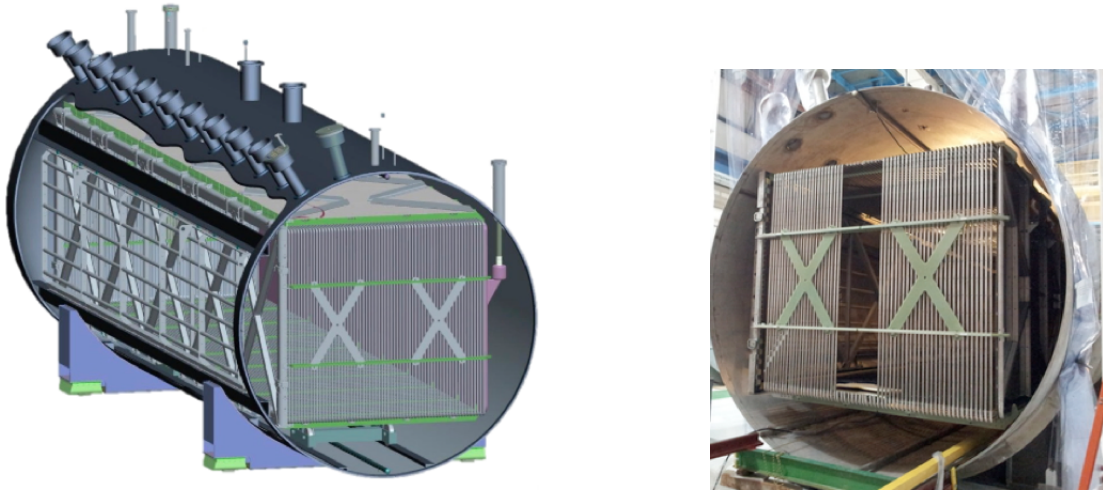


Figure 13: MicroBooNE the model and MicroBooNE the real man. (Right) Taken when the TPC was slid into the cryostat December 2013.

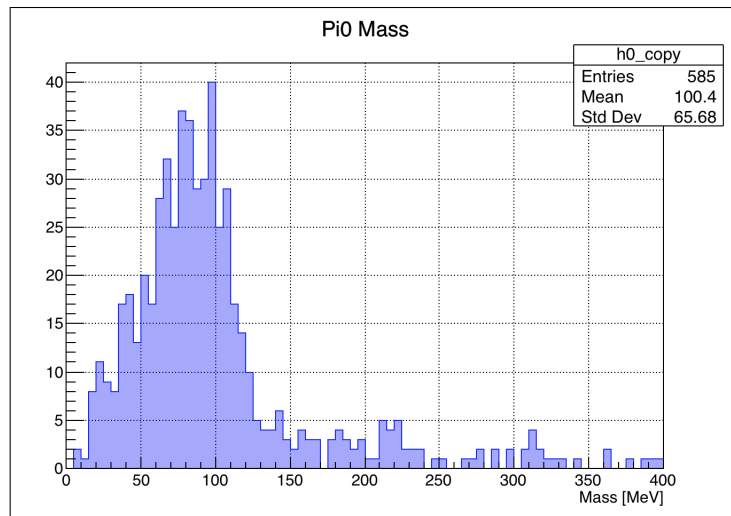
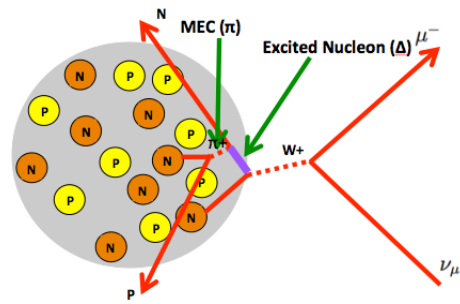
Figure 12: Calculated mass peak for the 585 selected CC π^0 events.

Figure 14: Charged Current event with nucleons interacting via Meson Exchange Current (MEC)

5 Event Selection

Now that we have an expectation for where our cross section should lie, we run our automated reconstruction and selection chains on the MC BNB + Cosmics samples referred to above, and attempt to retrieve this value. The first step in our automated selection is to run the ν_μ CC selection filter (SelectionII) developed for and since Neutrino 2016 [?]. SelectionII searches for events which have a track multiplicity of ≥ 1 , a μ candidate track which is either contained or uncontained, a flash of 50 PE in the beam window, an agreement in Z of the reconstructed flash and candidate muon. These criteria and several calorimetric and topological cuts are described in more detail in the ν_μ CC technote referenced above. The results of the filter are events with a μ candidate and an association between the reconstructed candidate track and pandora vertex. The most up to date filter (used here) currently has an efficiency of 42.3% and purity of 70.4%, and is described in DocDB 6172 [?]. This SelectionII efficiency pertains specifically to CC ν_μ inclusive events; to get a more precise idea of the efficiency of the filter on our signal of interest, we perform a short study on the MC BNB-only sample. As mentioned above, 3496 signal events from full BNB sample have a true vertex in the fiducial volume (FV); after Selection II, we are left with 1434 signal events in the FV. From these observations, we calculate our signal efficiency to be 41.0%, and will use this number rather than 42.3% in calculations for the rest of the note.

5.1 Hit Removal

At this point, we have a sample of events that are mostly CC ν_μ induced. From here, we must narrow down the sample of CC events we've selected with SelectionII to a sample that also contains a single π^0 . During past efforts, clustering has been somewhat of a bottle neck at which we lose many events due to the complexity of reconstructing complicated topologies all at once. In an attempt to mitigate this pitfall, we have chosen to add a hit removal stage. The goal of "hit removal" is to locate induced charge which 1) originates at the vertex and

2) is associated with a shower-like object in the event. Hit removal is broken into 2 stages: cosmic-induced and neutrino-induced. In the former, we remove charge produced by tracks tagged as cosmics by the pandoraCosmic algorithm and charge which is poorly aligned with the neutrino vertex. In the latter, we remove charge induced by neutrinos that has high local linearity (eg, charge induced by track-like particles). After hit removal we are ideally left with shower-like objects which seem to originate from the interaction vertex (Figure 15). More detail can be found in a previous technote [?].

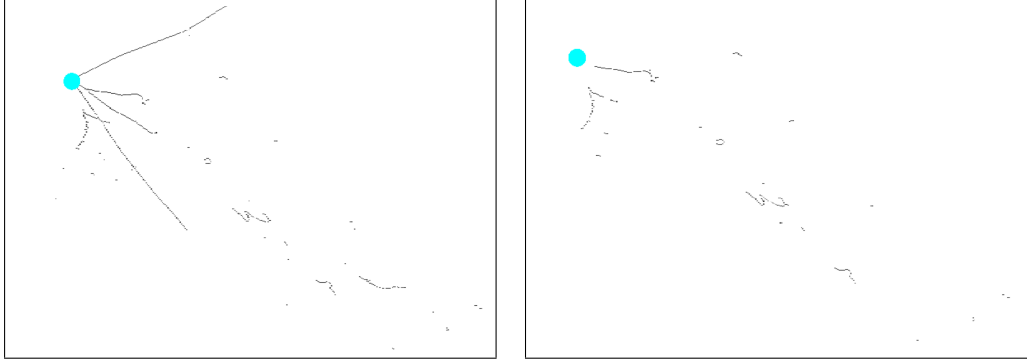


Figure 15: Vertex is depicted in cyan in both views. a) Before hit removal (left) and b) After hit removal (right) only shower-like hits originating from vertex remain.

5.2 $N\pi^0$ Filter

We can now use the shower-like hits we've identified in our Selection II output as a handle to select π^0 events. We approach this in the following way: first, we defined two sample sets on which to test the power of any filter we develop. The first set contains all final state π^0 events which originate from the Selection II candidate vertex (this includes both CC and NC), and the second contains everything else. From here, we build circles of various radii around the reconstructed vertex on an event-by-event basis. Using this circle we calculate both 1) the amount of shr-like charge from our previous step that falls within the radius and 2) the amount of total charge that falls within the circle. Ideally, the ratio of these 2 numbers will be higher for events that contain shower activity, as this information will be captured by the hit removal stage. We do this for a variety of radii, as shown in Figure 16.

We select a radius and ratio cut for our filter as follows: we want to consider the hit ratio at a radius after which most showers will have converted and deposited energy. As shown in Figure 16, lower radii up to roughly 35cm have notable number of π^0 entries in the 0 bin. Events in this bin have very few or no shower-like hits within the given radius, either due to longer conversion lengths or to hit track removal filtering more than it should be. To avoid losing events with longer conversion lengths and potentially creating a biased sample, we look to higher radii. We find that we maximize our efficiency * purity metric between 50 and 60 cm. We conservatively choose 60cm as our radius in order to maximize our metric and to maximize the range of radiation lengths that will make it through this filter. At 60cm, we found that the product of efficiency and purity was maximized at a ratio cut of 0.24 which preserves 70% of events in our sample with a primary π^0 with a purity of 36%. The results of this study can be seen in Figure 17.

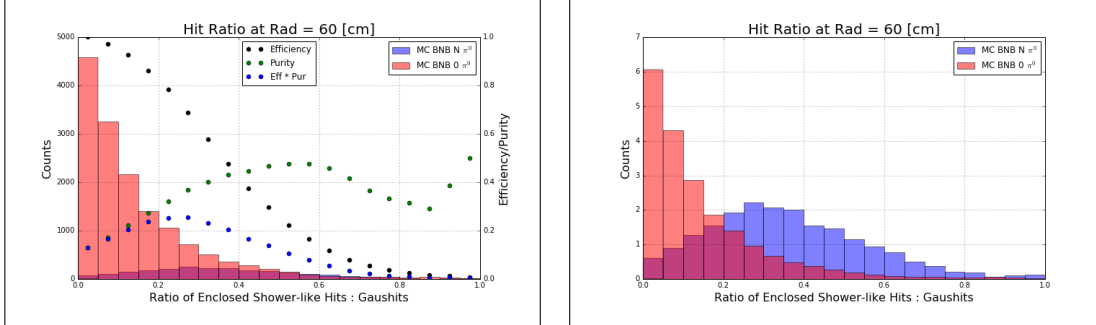


Figure 17: π^0 ratio plots constructed by taking the ratio of shower-like charge to total charge in radius = 60cm a) Absolute scale with corresponding efficiency, purity and product; b) Same plot area normalized to give a sense of the distribution shapes.

In attempt to improve the separation power of the filter, a second smaller study was performed. This study neglected the charge information associated with the tagged muon from the total charge pool. We hoped that this choice would push the $N-\pi^0$ event ratios further to the right while leaving the $0-\pi^0$ event ratios relatively unaffected. The results of this study can be seen in Figure 18. We found that while we are able to push the $N-\pi^0$ sample further right, the $0-\pi^0$ sample also spreads out and thus decreases our separation power. This is likely due to some mis-identification of shower hits in lower energy, shorter tracks. If some hits are mis-identified as shower-like in $0-\pi^0$ events, the resulting ratio without the tagged μ

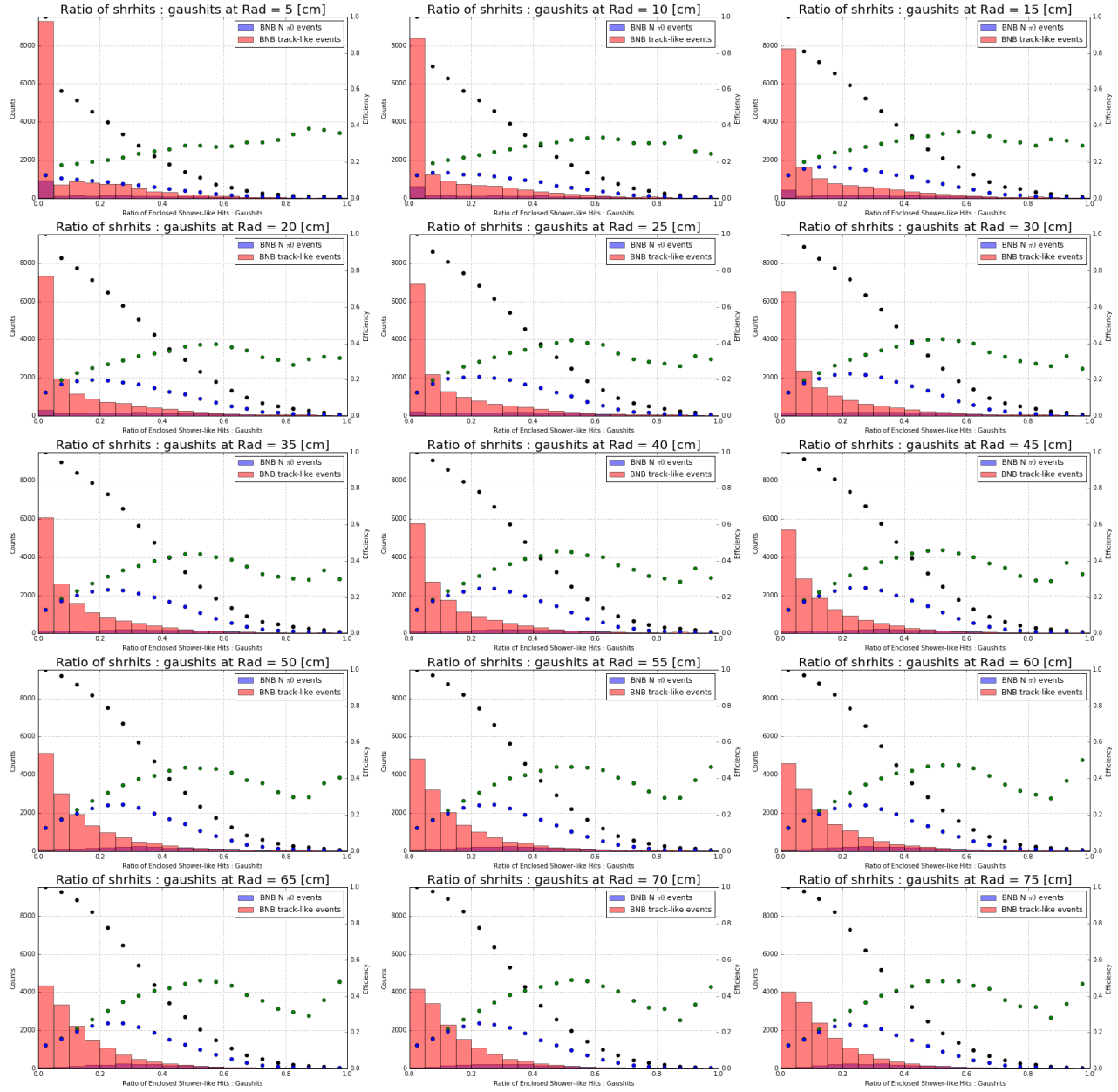


Figure 16: Ratio plots constructed by taking the ratio of shower-like charge to total charge at various radii.

hits gives the false impression of shower activity.

For the rest of the selection we will be using separation ratio value 0.24 obtained from the first study. A near-term future study will be done on MC in-time cosmics and triggered off-beam data events that pass SelectionII to ensure that this filter performs similarly enough between data and MC to use in a final analysis on data.

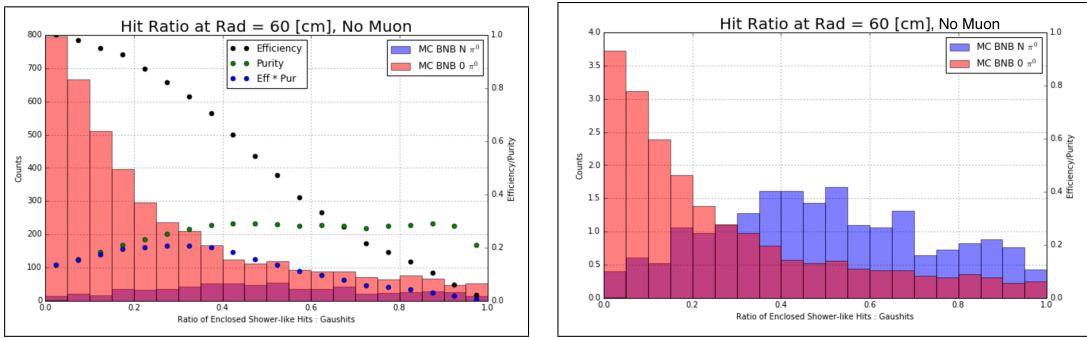


Figure 18: π^0 ratio plots constructed by taking the ratio of shower-like charge to total charge minus charge associated with the muon in radius = 60cm a) Absolute scale with corresponding efficiency, purity and product; b) Same plot area normalized to give sense distribution shapes.

6 Cross Section Calculation

6.1 True Cross Section

Our first step is to calculate the true flux-averaged cross section on Argon. We do this using 200k events from MCC7 BNB only simulation. The cross section can be calculated according to the following equation:

$$\sigma = \frac{N_{tagged} - N_{bkgd}}{\epsilon * N_{targ} * \phi} \quad (7)$$

where N_{tagged} , N_{bkgd} are the number of tagged events and background events respectively, ϵ is the efficiency, N_{targ} the number of targets and ϕ the flux.

We use a 200k MC BNB only sample to perform this initial calculation. Because we are using MC information to calculate a true value here, we use $\epsilon = 1$, $N_{bkgd}=0$ and $N_{tagged}=N_{signal}$. To calculate N_{signal} , we choose our volume of interest to be the Fiducial Volume (FV) used by SelectionII [?], with 20cm from the wall in X and Y, and 10cm from the wall in Z. We find $N_{tagged} = 3496$, for signal interaction vertices inside the FV. Note that while 200k events are simulated, more than half of these interactions occur outside the FV.

Our next job is to calculate the number of targets in our FV:

$$N_{targ} = \frac{\rho_{Ar} * V * Avogadro}{m_{mol}} \quad (8)$$

where ρ_{Ar} is the density of Liquid Argon, V is the volume of interest, and m_{mol} is the number of grams per mole of Argon. Using the FV as our volume of interest, we find:

$$N_{targ} = \frac{1.4[\frac{g}{cm^3}] * 4.25e7[cm^3] * 6.022e23[\frac{molec}{mol}]}{39.95[\frac{g}{mol}]} \quad (9)$$

(10)

$$= 8.969e29 \text{ molecular targets} \quad (11)$$

Our final step is to calculate the integrated flux. We do this by integrating over the ν_μ flux histogram (Figure 19) provided by the Beam Working Group [?], and normalizing by the POT in our sample. The POT is calculated by integrating over the POT of all subruns under consideration; in this case, our POT is 2.42e20. We calculate a total integrated flux of $1.20\text{e}11 \text{ cm}^{-2}$ over the range of 0.5 - 2.0 GeV (as was done by MiniBooNE) for $\langle E \rangle = 982 \text{ MeV}$. Putting it all together we find:

$$\sigma_{CC\pi^0} = \frac{3496}{1.20\text{e}11 \frac{1}{\text{cm}^2} * 8.969\text{e}29 \text{Ar}} \quad (12)$$

$$= (3.25 \pm 0.05) * 10^{-38} \frac{\text{cm}^2}{\text{Ar}} \quad (13)$$

$$= (3.25 \pm 0.05) * 10^{-38} \frac{\text{cm}^2}{\text{Ar}} \quad (14)$$

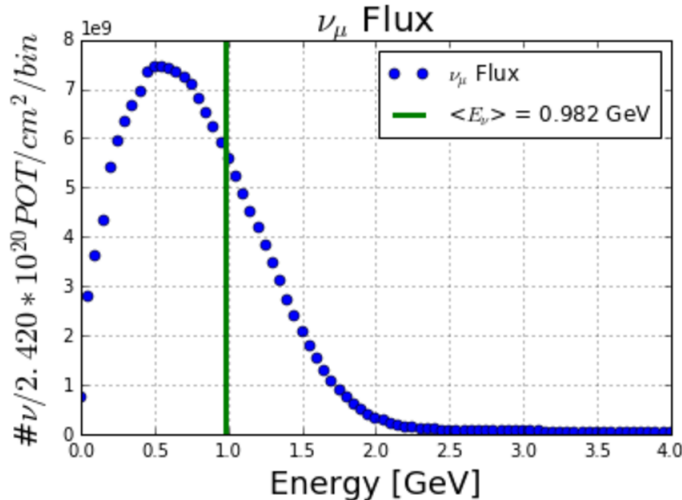


Figure 19: ν_μ Flux from Booster Neutrino Beam (BNB) at 470m

, where the error presented is purely statistical and dependent only on the number of signal events (for comparison with cross section measured on MC cosmics + BNB later). This result is in comparison to the MiniBooNE result of $\sigma_{CC\pi^0} = (9.2 \pm 0.3\text{stat.} \pm 1.5\text{syst.}) * 10^{-39} \frac{\text{cm}^2}{\text{CH}_2}$ at $\langle E_\nu \rangle_\phi = 0.965 \text{ GeV}$ [26]. Note that the MiniBooNE interaction medium is CH_2 , in contrast to the Ar in MicroBooNE. The comparison to Genie model over a variety

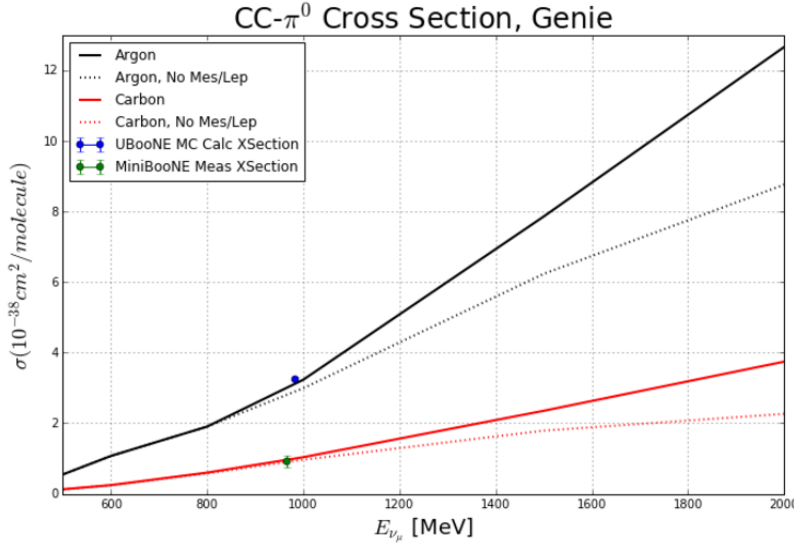


Figure 20: Genie calculated CC π^0 cross section. The cross sections are calculated at various energies for both Carbon and Argon, and for signal definitions that include mesons in the final state and those that don't. The MiniBooNE measured cross section is displayed along with the MicroBooNE MC calculated cross section.

of energies is shown in Figure 20.

6.2 Cross Section Calculation

We regroup at this point by summarizing the state of our candidate sample pool at each stage described so far in Tables 1 and 2. While our total number of reconstructed π^0 was 585 as described earlier, the final number of true CC π^0 events that we select is 254. The final efficiency is also calculated in this table to be 8.4%.

Table 1: Efficiency losses at each stage of selection

Step	Signal Events Remaining	Relative Efficiency	Total Efficiency
SelectionII	1244	100%	41.0%
N- π^0 Filter	872	70.1%	28.7 %
π^0 Reconstruction	254	20.4%	8.4%

Table 2: Breakdown of selected events

Total Reco'd π^0 Events	Signal	Background	Total Efficiency	Purity
585	254	331	8.4%	43.4%

Table 3: Breakdown of background events

Background	Percent of Sample
Clusters unrelated to π^0 reconstructed as π^0	23%
CC π^0 with mesons in final states	22%
NC π^0	21%
Mis-reconstructed vertex	11%
Multiple π^0	10%
Bad reconstruction (particles merged together)	4%
Secondary π^0	4%
N γ event	4%
Cosmic induced π^0	<1%

A breakdown of our sample backgrounds is summarized in Table 3. A few comments on these categories : First, the most dominant background is made up of events in which the 2 clusters contributing to the final reco'd " π^0 " are not both gamma-looking clusters. The most common instance of this is a OpenCV clustered track originating from the vertex, and another track or shower-like particle clustered elsewhere in the ROI. A study on conversion length (near 0 for tracks) vs cluster linearity was done, however, no strong correlations were found to further limit the contribution of these events; these studies are not currently included here. It is worth noting that many of these short tracks are protons, and could potentially be removed with a dEdx cut once we fully understand calibration. Second, the signal definition excludes events with mesons in the final state, and no studies have yet been done to specifically limit this background. As a result, these events make up a large chunk of our background, however track multiplicity and track length studies will be explored in the near future. Next, the category "bad reconstruction" refers specifically to events that contain 1 or more clusters that contain contributions from multiple particles (instances of

over-merging). Many of these reconstructed events with mistakes contain at least one very low energy "shower", and could be removed with a modest energy cut (20-30 MeV). There are also instances where the vertex is reconstructed in the wrong location (reco vertex > 5 cm from the true vertex location). In this instance, there are sometimes secondary π^0 's reconstructed at the incorrectly reconstructed vertex, and other times mis-clustering, or clusters unrelated to the π^0 being reconstructed as π^0 . Lastly, the secondary π^0 's that make it into this sample are those that are produced very near to the vertex, and so are not removed by our cluster alignment filter. With this information, we are now geared to calculate the CC π^0 cross section on MC cosmics + BNB using Equation 7. Noting that the POT for this sample was 1.9e20, we find:

$$\sigma_{CC\pi^0} = \frac{585 - 331}{0.084 * 9.438e10 \frac{1}{cm^2} * 8.969e29 Ar} \quad (15)$$

$$= (3.57 \pm 0.34) * 10^{-38} \frac{cm^2}{Ar} \quad (16)$$

$$= (3.57 \pm 0.34) * 10^{-38} \frac{cm^2}{Ar} \quad (17)$$

The error shown here is purely statistical and calculated using only N_{tagged} and N_{bkgd} . This comparison is within 1σ of the MC cross section, calculated to be $(3.25 \pm 0.05) * 10^{-38} \frac{cm^2}{Ar}$.

A Appendix

In the 2 neutrino oscillation model, we represent a flavor state as the linear combination of mass eigenstates via a unitary matrix

$$|\nu_x\rangle = \sum_{j=1,2} U_{ij} |\nu_j\rangle \quad (18)$$

A 2 dimensional unitary rotation matrix can be written as

$$U = \begin{bmatrix} \cos(\theta) & \sin(\theta) \\ -\sin(\theta) & \cos(\theta) \end{bmatrix} \quad (19)$$

Using this unitary matrix, we can re-write equation 17

$$\begin{bmatrix} \nu_\alpha \\ \nu_\beta \end{bmatrix} = \begin{bmatrix} \cos(\theta) & \sin(\theta) \\ -\sin(\theta) & \cos(\theta) \end{bmatrix} \begin{bmatrix} \nu_1 \\ \nu_2 \end{bmatrix} \quad (20)$$

In order to put equation 19 into a more meaningful form, it is useful to put both sides into flavor basis. To start this process, we recall that we can use the time propagator to represent evolution in time. For simplicity, we also re-write the $Et - \vec{p} \cdot \vec{x}$

$$\begin{bmatrix} \nu_1(t) \\ \nu_2(t) \end{bmatrix} = \begin{bmatrix} e^{-i\phi_1} & 0 \\ 0 & e^{-i\phi_2} \end{bmatrix} \begin{bmatrix} \nu_1(0) \\ \nu_2(0) \end{bmatrix} \quad (21)$$

Then, using the inverse of equation 19, we can rewrite

$$\begin{bmatrix} \nu_1(0) \\ \nu_2(0) \end{bmatrix} = \begin{bmatrix} \cos(\theta) & -\sin(\theta) \\ \sin(\theta) & \cos(\theta) \end{bmatrix} \begin{bmatrix} \nu_\alpha(0) \\ \nu_\beta(0) \end{bmatrix} \quad (22)$$

Combining equations 19, 21, we can represent time propogated flavor basis as

$$\begin{bmatrix} \nu_\alpha(t) \\ \nu_\beta(t) \end{bmatrix} = \begin{bmatrix} \cos(\theta) & \sin(\theta) \\ -\sin(\theta) & \cos(\theta) \end{bmatrix} \begin{bmatrix} e^{-i\phi_1} & 0 \\ 0 & e^{-i\phi_2} \end{bmatrix} \begin{bmatrix} \cos(\theta) & -\sin(\theta) \\ \sin(\theta) & \cos(\theta) \end{bmatrix} \begin{bmatrix} \nu_\alpha(0) \\ \nu_\beta(0) \end{bmatrix} \quad (23)$$

Instead of simplifying this any further, we look at a test case. Assume a beam is produced in a pure ν_β state at $t=0$. To find the probability that at time t a ν_β in the beam has oscillated into a ν_α , we calculate the square of the probability amplitude:

$$\begin{aligned} |<\nu_\beta(0)|\nu_\alpha(t)>|^2 &= |<\nu_\beta(0)|\cos\theta\sin\theta(e^{-i\phi_1} - e^{-i\phi_2})|\nu_\beta(0)>|^2 \\ &= (\cos\theta\sin\theta)^2(1 + 1 + e^{i(\phi_1-\phi_2)} + e^{-i(\phi_2-\phi_1)}) \\ &= 2(\cos\theta\sin\theta)^2(1 - \cos(\phi_1 - \phi_2)) \\ &= \sin^2 2\theta \sin\left(\frac{\phi_1 - \phi_2}{2}\right) \end{aligned} \quad (24)$$

At this point, our probability formula is almost in its familiar form. To finalize, we recall from above that the phase shift ϕ is $E_i t - p_i x$ and make the following assumptions:

- 1) At $v \sim c$, $x \sim t \sim L$
- 2) Mass eigen states are created with equal energy Now ϕ_i can be written

$$\begin{aligned} \phi_i &= (E - p_i)L \\ \text{where } p_i &\approx E\left(1 - \frac{1}{2}\frac{m_i^2}{E}\right) \\ \implies \phi_2 - \phi_1 &= \frac{1}{2}\frac{L}{E}(\Delta m_2^2 - \Delta m_1^2) \end{aligned} \quad (25)$$

which leads us to the probability of oscillation from ν_β to ν_α :

$$P(\nu_\beta \rightarrow \nu_\alpha) = \sin^2(2\theta)\sin\left(\frac{1}{4}\frac{L}{E}\Delta m_{12}^2\right) \quad (26)$$

References

- [1] Davis, Raymond, and Don S. Harmer. "Solar Neutrinos." *Solar Neutrinos*. (1964): n. page. Print.
- [2] Cleveland, Bruce T., et al. "Measurement of the Solar Electron Neutrino Flux with the Homestake Chlorine Detector." *ApJ*. 496.505 (1998): n. page. Print.
- [3] Hirata, K. S., et al. "Real-time, directional measurement of 8 solar neutrinos in the Kamiokande II detector." *Phys. Rev. D*. 44.2241 (1991): n. page. Print.
- [4] Hampel, W., et al. "GALLEX solar neutrino observations: Results for GALLEX IV." *Phys. Lett. B*. 447. (1999): 127-133. Print.
- [5] Hampel, W., et al. "Final results of the ^{51}Cr neutrino source experiments in GALLEX." *Phys. Lett.* 420.1-2 (1998): 114-126. Print.
- [6] Abdurashitov, J. N., et al. "The Russian-American Gallium Experiment (SAGE) Cr Neutrino Source Measurement." *Phys. Rev. Lett.* (1996): n. page. Print.
- [7] Fukuda, Y., et al. "Evidence for Oscillation of Atmospheric Neutrinos." *Phys. Rev. Lett.* (1998): n. page. Print.
- [8] Clarke, Arthur C. *The Songs of Distant Earth*. Del Rey Books, 1986. Print.
- [9] McGregor, Gordon A. "FIRST RESULTS FROM THE SUDBURY NEUTRINO OBSERVATORY." *arXiv*. (2002): n. page. Print.
- [10] Adamson, P., et al. "Measurement of Neutrino and Antineutrino Oscillations Using Beam and Atmospheric Data in MINOS." *Phys. Rev. Lett.* 110.251801 (2013): n. page. Print.
- [11] Boyd, Steve. "Neutrino Oscillations." PX435 Neutrino Physics. N.p.. Web. 19 Feb 2015.
http://www2.warwick.ac.uk/fac/sci/physics/current/teach/modulei_home/px435/lec_oscillations.pdf

- [12] MiniBooNE Collaboration. "The Neutrino Flux prediction at MiniBooNE." Phys. Rev. D. (2008): n. page. Print.
- [13] Aguilar, A., et al. "Evidence for Neutrino Oscillations from the Observation of Electron Anti-neutrinos in a Muon Anti-Neutrino Beam." Phys. Rev. D. (2001): n. page. Print.
- [14] Szlec, A. M. "Recent Results from ArgoNeuT and Status of MicroBooNE." Proceedings from Neutrino 2014. (2014): n. page. Print.
- [15] Anderson, Colin. "Measurement of Muon Neutrino and AntiNeutrino Induced Single Neutral Pion Production Cross Section." Thesis. (2011): n. page. Print.
- [16] Caratelli, D., et al. "Electron Neutrino Cosmogenic Background Mitigation in MicroBooNE." Technote 3978. (2014): n. page. Print. http://www-microboone.fnal.gov/at_work/technotes.html.
- [17] Nakayama, S., et al. "Measurement of single π^0 production in neutral current neutrino interactions with water by a 1.3 GeV wide band muon neutrino beam." Phys. Lett. B. 619.255-262 (2004): n. page. Print.
- [18] Kurimoto, Y., et al. "Measurement of inclusive neutral current 0 production on carbon in a few-GeV neutrino beam." Phys. Rev. D. 81. (2010): n. page. Print.
- [19] Aguilar, A., et al., *The Neutrino Flux at MiniBooNE*,
<https://arxiv.org/pdf/0806.1449v2.pdf>
- [20] S. B. Barish et al., Phys. Rev. D., 19, 2521 (1979).
- [21] G. M. Radecky et al., Phys. Rev. D., 25, 1161 (1982)
- [22] T. Kitagaki et al., Phys. Rev. D., 34, 2554 (1986)
- [23] D. Allasia et al., Nucl. Phys. B., 343, 285 (1990).
- [24] H. J. Grabosch et al., Zeit. Phys. C., 41, 527 (1989).

- [25] J. Catala-Perez, *Measurement of neutrino induced charged current neutral pion production cross section at SciBooNE*. <https://inspirehep.net/record/1280829?ln=en>
- [26] A. A. Aguilar-Arevalo, et al., *Measurement of ν_μ -induced charged-current neutral pion production cross sections on mineral oil at $E_\nu = 0.5\text{-}2.0 \text{ GeV}$* ,
<https://arxiv.org/pdf/1010.3264v4.pdf>
- [27] Robert H. Nelson, Thesis, *A Measurement of Neutrino-Induced Charged-Current Neutral Pion Production*,
https://www-boone.fnal.gov/publications/Papers/rhn_thesis.pdf
- [28] Joan Catala Perez, Thesis, *Measurement of neutrino induced charged current neutral pion production cross section at SciBooNE.*,
<http://lss.fnal.gov/archive/thesis/2000/fermilab-thesis-2014-03.pdf>
- [29] Jose Luis Palomino Gallo, Thesis, *First Measurement of $\bar{\nu}_\mu$ of Induced Charged-Current π^0 Production Cross Sections on Polystyrene at $E_{\bar{\nu}_\mu} 2\text{-}10 \text{ GeV}$* ,
<http://inspirehep.net/record/1247736/files/fermilab-thesis-2012-56.pdf>
- [30] *Single neutral pion production by charged current $\bar{\nu}_\mu$ interactions on hydrocarbon at $< E_\nu > = 3.6 \text{ GeV}$* ,
<http://www.sciencedirect.com/science/article/pii/S0370269315005493>
- [31] C. Mariani, et al., *Measurement of inclusive π^0 production in the Charged-Current Interactions of Neutrinos in a 1.3-GeV wide band beam*,
arXiv:1012.1794
- [32] The MicroBooNE Collaboration, *Design and Construction of the MicroBooNE Detector*,
<https://arxiv.org/pdf/1612.05824v2.pdf>